RSC Advances

PAPER

View Article Online
View Journal | View Issue

Cite this: *RSC Adv.*, 2026, **16**, 16030

Anisotropic water sliding radiative cooling emitter for atmospheric water harvesting

Kai Gao, [a] JiajiaWu,*[a] Jinze Li*[b] and Luanhong Sun[c]

Water shortage is a major problem for human society in the 21st century. Radiative cooling-based atmospheric water harvesting (AWH) has emerged as a promising strategy to address this crisis. Hydrophilic surfaces are known to facilitate water vapor condensation, but a water film that adheres tightly to the radiative cooling emitter (RCE) will severely reduce water collection flux. Hydrophilic surfaces with low sliding angles are highly desirable for high-performance AWH, but achieving both sufficient hydrophilicity and a low sliding angle is inherently contradictory in conventional surface designs. In this work, we report a mass-producible silicon-based hydrophilic RCE with anisotropic low sliding angles. We fabricated composite microstructures consisting of grooves and pockets on a diamond-wire-cut silicon substrate by combining metal-assisted chemical etching with a rounding treatment. The structured surface was then modified *via* a specially designed localized hydrophilic treatment. The introduction of nano-pockets trapped a large number of air bubbles at the interface between water droplets and the RCE, which effectively reduced the water sliding angle. The as-prepared anisotropic RCE exhibited a water contact angle of 60.2° and an ultra-low water sliding angle of only 31°. Experimental results demonstrated that the proposed RCE enables efficient AWH for more than 17 hours per day, with a maximum water mass flux of 38.2 g m^{-2} h^{-1}. This performance is 71% higher than that of a control group with a comparable emissivity.

Received 25th November 2025
Accepted 10th March 2026

DOI: 10.1039/d5ra09103a

rsc.li/rsc-advances

1 Introduction

Effective methods for obtaining freshwater is always a hot topic in arid regions. Current mainstream research on desalination technologies prioritizes addressing core technical bottlenecks, such as concentration polarization, long-term salt accumulation on functional surfaces, and mechanical degradation of desalination materials under high-salinity conditions, alongside the development of scalable, low-cost fabrication processes for high-performance desalination components to support industrial deployment.[1–3] However, existing methods such as seawater desalination require substantial energy, can only be carried out in coastal areas, and cannot benefit inland areas that are truly water-scarce. Therefore, researchers have turned to water vapor in the atmosphere.[4–7] Methods of collecting water from the atmosphere can be divided into two categories. One method involves substances that can be used to adsorb water vapor; then, liquid water can be collected by heating and desorption.[8,9] This process consumes a lot of energy, and the water harvesting efficiency is inadequate. The other method involves condensing the water vapor in the air into liquid water using cold sources[10] or dewing collectors.[11,12] The artificially manufactured cold source still relies on additional energy consumption. The efficiency of dew collectors depends on special environmental conditions. Given the exceptionally high demand for freshwater, the costs of desalination and AWH technologies based on electrically driven cold sources are economically prohibitive against the backdrop of energy shortages.[13] In light of these constraints, AWH relying on spontaneous radiative cooling has emerged as a promising alternative solution. Radiative cooling originates from the imbalance in thermal radiation between the emitter and the cold source. All objects spontaneously generate heat radiation to dissipate energy, and the wavelength of thermal radiation is concentrated in the range of 8–13 μm for objects at room temperature. Because the earth's atmosphere is almost transparent to electromagnetic waves in the wavelength range of 8–13 μm, called the "atmosphere window", the thermal radiation of the emitter reaches the space where the temperature is only 3 K, resulting in the spontaneous radiative cooling.[14] In recent years, various high-performance RCEs have been reported, and daytime radiative cooling has also been achieved.[12–18] Moreover, the RCE has been utilized as the cold source in AWH without consuming energy.[19–22] Table 1 presents recent advancements in

[a]*College of Physics and Information Engineering, Minnan Normal University, 36 Zhiqian Ave, Zhangzhou 363000, People's Republic of China. E-mail: wujiajia17@mails.ucas.ac.cn*

[b]*College of Integrated Circuit Science and Engineering, Nanjing University of Posts and Telecommunications, 9 Wenyuan Road, Nanjing 210023, People's Republic of China. E-mail: lijinze@njupt.edu.cn*

[c]*School of Materials Engineering, Jinling Institute of Technology, Nanjing 211169, China*

Table 1 Recent works in radiative cooling AWH

Serial number	Radiative emitter	Approach	AWH mass flux
This work	Silicon nanostructure	Condensation	38.2 g m^{-2} h^{-1}
2	PDMS-TiO_2 (ref. 23)	Condensation	916.6 g m^{-2} h^{-1}
3	PDMS-Al[24]	Condensation	21 g m^{-2} h^{-1}
4	PDMS + SiO_2 + reflector[25]	Condensation	50 g m^{-2} h^{-1}
5	PDMS + solar absorber[26]	Solar heat + condensation	3654 g per m^2 per day
6	Composite hydrogel[27]	Adsorption	0.310 kg m^{-2} h^{-1}
7	Cellulose scaffold -LiCl[28]	Adsorption	6.75 L per kg per day
8	Fabric[29]	Adsorption	1.29 kg kg^{-1}

AWH based on radiation cooling, including condensation, heating condensation and adsorption. It should be noted that the AWH performance reported in different studies is often difficult to compare directly due to the fact that it is influenced by various factors. For example, organic aerosols and their aging processes modulate regional atmospheric humidity and water vapor nucleation properties, which are non-negligible environmental factors affecting atmospheric water harvesting efficiency.[30–36]

Nonetheless, it is not enough to just pursue distinguished radiative cooling performance in AWH.[19,22,37] In the process of condensation, a water film is formed on the surface of the emitter, thereby hindering the heat transfer between the emitter and the moist air. Because water has a strong absorption of mid-infrared heat radiation, the coverage of the water film also changes the emissivity of the emitter surface.[38] Therefore, the water film has a negative impact on both the cooling performance of the emitter and the water mass flux of AWH. Two approaches to solving the problem have been reported. One is to remove the water film by mechanical scraping,[39,40] which will bring additional system complexity, cost and energy consumption. The other is to employ a super-hydrophobic surface to make water films fall off spontaneously. Haechler *et al.*[22] prepared a super-hydrophobic carbon nanofiber coating as a super-hydrophobic film on the back of the PDMS-Al emitter, realizing 24-hour uninterrupted AWH, with a water mass flux of 50 g m^{-2} h^{-1}. Unfortunately, the super-hydrophobic surfaces make the nucleation of water droplets on the emitter surface difficult, thereby reducing the efficiency of AWH.[25,37]

Simulation results have shown that a surface with small hydrophilic protrusions on a hydrophobic substrate has better water collection performance.[41] The hydrophilic low-sliding surface is the ideal pursuit of RCEs for AWH. Andrew *et al.*[41] reported that the Namib desert beetle whose elytra feature randomly distributed hydrophilic protrusions atop a super-hydrophobic background. Water vapor from humid ambient air condenses preferentially on the hydrophilic convex protrusions of the elytra; the resulting droplets grow gradually until reaching a critical volume, at which point they detach rapidly, slide into the superhydrophobic grooved regions, and roll down the surface. Thus, efficient water collection is realized by reciprocating the condensation-growth-sliding process. Inspired by the unique functions of pitcher plants and rice leaves, Dai *et al.*[42] presented a hydrophilic directional slippery, rough surface that is capable of rapidly nucleating and removing water droplets. Hydrophilic directional slippery rough surfaces can outperform their hydrophobic counterparts and nonlubricated super-hydrophobic surfaces in both droplet nucleation and mobility during dropwise condensation and fog harvesting processes. According to the bionic research results,[13,42–48] surface structures and functional groups are key factors in determining the adhesion or sliding state of the droplets. The combination design of a hydrophobic substrate and hydrophilic nano-protrusions has been proven to be extremely effective, especially in the case of the low-temperature differences between the ambient and the cold source. However, surfaces work for AWH need to be precisely designed and then fabricated using precision manufacturing methods, which increases the cost and limits their potential to be widely used.

To achieve the efficient preparation of the above structures in a simple and inexpensive way, silicon microstructures, which have been extensively studied and applied in a variety of fields, have attracted our attention.[43–49] For example, specially designed microstructures can achieve enhanced absorption of incident light and are generally applied in light-trapping surfaces. The effective working wavelength of silicon-based microstructures depends on the size, distribution and shape of the structures, and preeminent light absorption in a wide range of wavelengths and incident angles can be achieved.[50–58] If it can achieve efficient light trapping in the atmospheric window band, radiative cooling would occur. With the gradual maturity of cheap preparation methods such as metal-assisted chemical etching (MACE),[59,60] the cost of silicon microstructures has dropped significantly. More importantly, the pure silicon substrate is hydrophobic, and the microstructures may be specially designed to meet the requirements for hydrophilic performance; it may be a satisfactory choice for achieving radiative cooling and efficient AWH at night. Although the pursuit of pure night time radiative cooling has gradually diminished with the emergence of daytime radiative cooling, the situation is different for the emitters used for AWH. In the daytime, solar radiation weakens the radiative cooling temperature difference, and the relative humidity of the air is usually inadequate in most cases, which results in low efficiency of AWH. Therefore, the pursuit of all-day radiative cooling brings limited improvement of AWH efficiency in most cases. Another way is to find cheap and efficient RCEs. Silicon microstructures are manufactured *via* well-established, scalable fabrication

routes and enable precise control over surface topological features, demonstrating strong application potential for AWH systems. Our core goal is to achieve viable AWH efficiency through an ultra-low-cost method compatible with large-scale industrial replication. Implementing high-reflectance nanostructures would significantly increase the manufacturing complexity and cost, conflicting with our objective of accessible, scalable AWH technology.

In this work, we demonstrated the feasibility and advantages of a hydrophilic anisotropic sliding surface as the RCE for AWH. An RCE with asymmetric sliding angles was prepared by the MACE method based on the commercial diamond wire cutting silicon wafers, greatly improving the mass flux of AWH. Surface microstructures and localized hydrophilic treatment are pivotal to realizing the asymmetric sliding angle of water droplets. Benefiting from abundant silicon wafers and a simple fabrication process, the RCE is suitable for mass production and application.

2 Results and discussion

2.1 Self-sliding AWH based on RCE

Here are four energy exchange mechanisms between the RCE and the environment (Fig. 1(a)). The thermal radiation (P_r) of RCE can pass through Earth's atmosphere and reach outer space directly. The environment is full of thermal radiation, so the RCE will absorb it to heat up (P_a). Because of the temperature difference between the RCE and the environment, there is a non-radiative heat-exchange power (P_n). Solar radiation also has a significant impact on the temperature of RCE (P_s). The net cooling power (P_{net}) of RCE is as follows:

$$P_{net} = P_r - P_a - P_n - P_s \quad (1)$$

As shown in Fig. 1(b), the solar spectrum range is 0.3–2.5 μm, and the power of the AM1.5 is 1000 W m^{-2}, while the theoretical power P_r of an ideal RCE is only 146 W m^{-2}. The radiative cooling power can only offset 14.6% of the solar absorption. It is essential to have both high reflection performance in the solar spectral region and high emissivity performance in the atmospheric window band for all-day RC, which limits the choices of RCEs. In the daytime, the radiative cooling temperature difference tends to be insufficient to maintain a stable AWH due to the absorption of solar energy. The pursuit of daytime AWH has pushed up the cost and device complexity of RCEs. The temperature difference in night radiative cooling is higher, and the design of the corresponding RCE is also simpler, only needing to focus on increasing the RCE emissivity of the atmospheric window band. If only pursuing an efficient AWH process at night, more free space for RCE performance optimization and cost control could be obtained with an acceptable AWH performance loss.

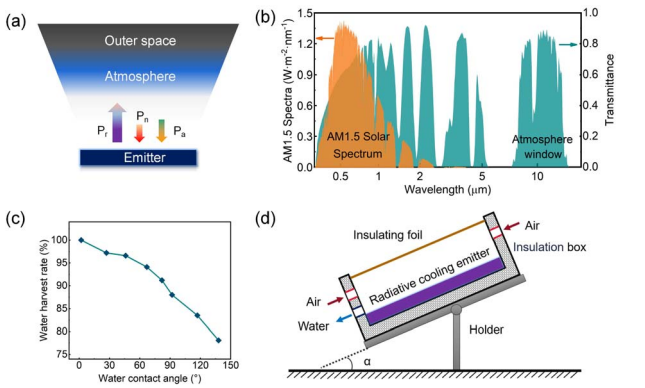

Fig. 1 (a) Schematic of radiative cooling; (b) AM1.5 standard solar spectrum and transmittance of the atmosphere; (c) AWH efficiency on surfaces with different water contact angles with a temperature difference of 15 °C and air humidity of 75%; (d) schematic of the AWH experimental device.

For AWH based on RCE, the water contact angle of RCE has a significant influence. When the partial pressure of water vapor in the air is not saturated, the adsorbing and escaping processes of water molecules exist on the RCE surface at the same time. Excellent surface hydrophilicity can improve the adsorption efficiency of water molecules on the emitter surface, thereby promoting AWH.[23] To prove this, a verification experiment was conducted. Water contact angles were adjusted by depositing different coatings on polished Al substrates (detailed information can be found in Table S1). Modules of thermoelectric cooling devices were applied on the back of Al substrates as the cold sources to ensure that the temperature of the cold sources is equal and stable. The condensed water film is mechanically wiped periodically. The AWH performance of surfaces with different hydrophilicity, *i.e.*, contact angles, was tested as shown in Fig. 1(c). When the contact angle increases to 140°, the water mass flux of AWH is only 78% of that when the contact angle is 3°. Water droplets will be gripped by hydrophilic surfaces and hinder the further progress of the AWH in the absence of a mechanical water removal device. Therefore, the RCE is designed to be inclined in the AWH experiment, so that the water droplets can roll off spontaneously. An experimental device scheme, as shown in Fig. 1(d), was applied to test the AWH performance of RCEs. The RCE was placed in a thermal insulation box made of thermal insulation foam. There were channels on the side walls of the box for air to enter and for condensate water to flow out. The device was placed on a holder that can freely adjust the inclination angle.

2.2 Fabrication and performance of silicon-based RCE

A hydrophilic RCE with a low water sliding angle is the ideal choice for AWH, but sufficient hydrophilicity and low sliding angle seem to be contradictory. The combined structure of micro-grooves + nano-pockets reported in this work successfully resolves this contradiction. Oxidized hydrophilic nano-protuberances enhance the surface roughness of RCE, thereby enhancing the hydrophilicity of the RCE. On the other hand, the nested structure introduces lots of air pockets on the hydrophobic silicon substrate, which is very helpful for reducing the water sliding angle in the groove direction. Sufficient hydrophilicity and a low sliding angle are achieved at the same time

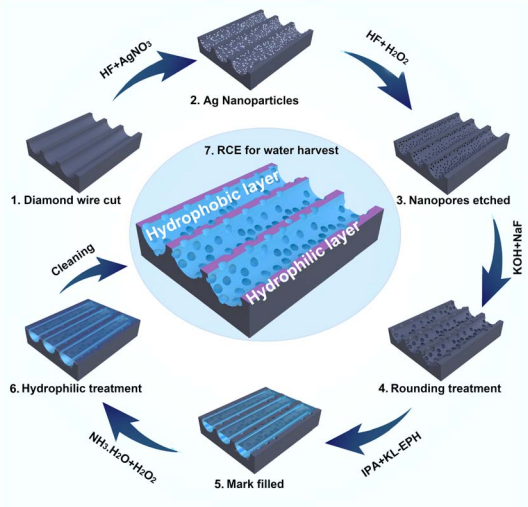

Fig. 2 Schematic of the preparation process of the anisotropic RCE.

on a specially fabricated RCE surface. The preparation process of the RCE is shown in Fig. 2 and Table 2. Silicon wafers cut by diamond wire were employed as substrates. The diamond wire cut method has been widely used in the silicon solar cell industry because they are inexpensive and readily available, thus helping to reduce the manufacturing cost of our RCE. Cutting marks were distributed along the grinding movement direction on the silicon wafer surface (SEM images of the substrate shown in Fig. S1 in the SI). A two-step method was adopted in this work. First, a mixed solution of $AgNO_3$ + HF was employed to obtain the precursor layer. Ag^+ ions undergo a reduction reaction to generate Ag particles attached to substrates. The samples were then placed in the HF + H_2O_2 solution for etching. In the etching solution, the Ag nanoparticles and the nearby silicon substrate form a local galvanic cell, resulting in a faster etching rate in the area covered by the Ag nanoparticles. Randomly distributed deep nanopores were formed (SEM images of nanopores shown in Fig. S2 in the SI). For the Ag MACE process, the preferred etching direction is [001], so all nanopores are vertically downward. Next, the silicon substrate was immersed in a KOH/NaF mixed solution for rounding treatment. The nanopore structures shown in step 3 can be regarded as a damaged layer, and the rounding process will increase the pore diameter of the nanopores and thin the damaged layer. A nested structure of line-shaped deep grooves + nanopores was formed. The local oxidation/hydrophilic treatment process is the key to achieving hydrophilic low-slip angle surfaces. The surface of the sample was coated with a mixed solution of isopropylamine (IPA) + 2-phenoxyethanol (KL-EPH). The mixed solution on the sample surface was properly evaporated to ensure that the residual liquid filled the deep groove structure. The coated samples were placed in a solution of NH_3 H_2O + H_2O_2 for hydrophilic treatment. The deep grooves were filled with IPA + KL-EPH solution to avoid oxidation and maintain a hydrophobic state. The protruding part shown after step 5 is in a hydrophilic state due to being oxidized. Finally, the structure shown in step 7 was formed.

Fig. 3(a)–(c) show the SEM images of the surface structure of the RCE after the rounding treatment for different durations. When the rounding time is 5 min, there are many small protuberances on the surface of the RCE, and the cutting marks are also deep grooves. If the rounding time is extended to 20 min, the depth of the surface structure decreases, and the surface becomes smoother. A groove-pocket nesting structure

Table 2 Experimental design

Step	Process	Parameters/items/instruction
1	Silicon wafers cut by diamond wire	Purchased from Trina Solar Co
2	Ag nanoparticles deposition	Samples were immersed in the $AgNO_3$ (0.02 mol L^{-1})/HF (4 mol L^{-1}) solution for 10 s
3	Nanopores etching	Samples were immersed in the HF (5.4 mol L^{-1})/H_2O_2 (3.5 mol L^{-1}) solution for 1 min
4	Rounding treatment	Samples were immersed in the KOH (0.04 mol L^{-1})/NaF (0.16 mol L^{-1})/isopropyl alcohol (IPA, 5 vol%) solution for rounding treatment for 5–40 min at 35 °C
5	Mark filled	Samples were coated with a mixed solution of IPA + ethylene glycol monophenyl ether (KL-EPH)
6	Hydrophilic treatment	A mixed solution of NH_3 H_2O (15 vol%)/H_2O_2 (15 vol%)/H_2O was used for hydrophilic treatment for 0–10 min
7	Performance measurement	Radiative cooling performance (outdoor, clear night, 23 ± 1 °C, RH 75% ± 5%) and water contact performance (sliding angle and contact angle) were measured
8	AWH measurement	AWH measurement was carried out outdoors on a wind-free sunny day. (0–24 h, 25 ± 2 °C, RH 75% ± 5%, wind speeds 0.4 ± 0.1 m s^{-1}, dew points 17 ± 1 °C)

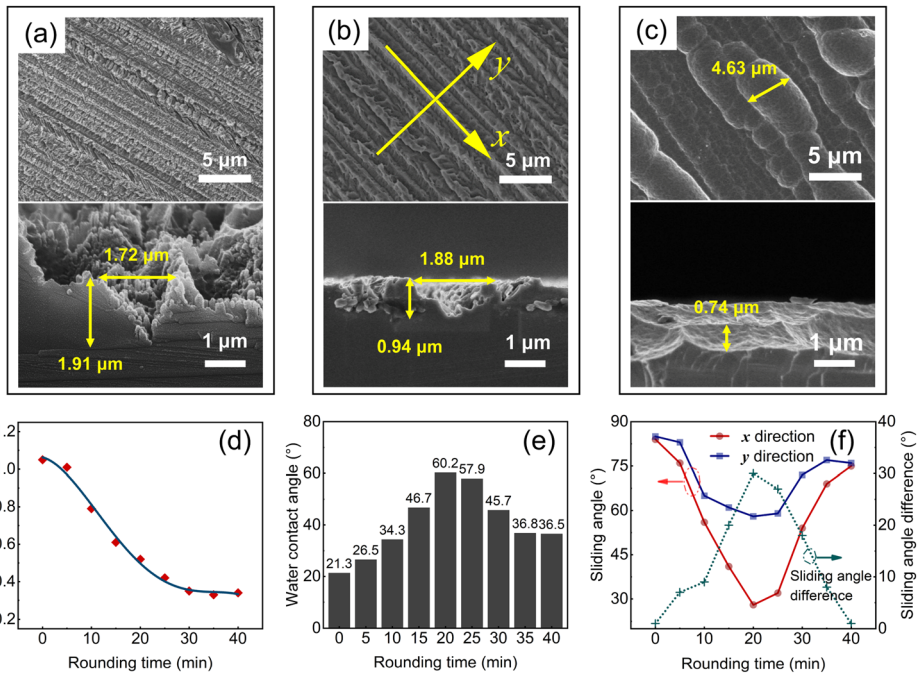

Fig. 3 Top view and cross-sectional SEM images of anisotropic RCE samples with rounding treatment durations of 5 min (a), 20 min (b) and 40 min (c); changes in the surface roughness (d), water contact angle (e) and water sliding angle (f) with rounding treatment time; the dotted line in (f) is the difference in the water sliding angle in the *x* and *y* directions.

appears. As the rounding treatment continues, cutting mark density decreases, the structure depth becomes shallower, and the surface roughness of the sample also decreases (as shown in Fig. 3(d)). The water contact angle and emissivity of the RCE are related to its surface roughness. A smooth surface will bring a non-oriented water sliding angle and lower infrared emissivity. This means that the emitter has experienced overall performance degradation.

Contact angles and sliding angles of samples after hydrophilic treatment for 5 min are shown in Fig. 3(e) and (f), respectively. The water contact angle of the RCE surface first increases and then drops with the extension of the rounding treatment. Correspondingly, the change in sliding angle is the opposite. Air-pocket structures inside grooves expand, resulting in a sharp drop in the sliding angle along the cutting mark direction (*x*-direction). Due to the obstruction of cutting marks in the *y*-direction, the decline rate of the sliding angle in the *x*-direction is much greater than in the *y*-direction. Air pockets help water droplets to slide more and more easily along the groove direction. The blocking effect of grooves on sliding water droplets always works. The directional sliding angle difference reached a maximum of 31° for the rounding treatment of 20 min, but if the rounding reaction continues, cutting marks and air pockets are both destroyed, so the sliding angles along the *x*- and *y*-directions tend to be the same. (Marks densities and structure depths with different rounding treatment durations are given in Fig. S3 in the SI).

The water contact angle images of three samples with rounding durations of 5 min, 20 min and 40 min are given in Fig. 4. When the rounding time is 5 min, the RCE surface is rough. Due to the insufficient size of nano-protuberances, effective air pockets cannot be formed. The entire surface is oxidized in the hydrophilic treatment. Nanostructures provide lots of attachment sites for the micro-droplets due to their hydrophilic state.

2.3 Mechanism of anisotropic water sliding of RCE

The water contact in the situation satisfies the Wenzel condition.[43,61,62] When the solid surface is a hydrophilic rough surface, nano-protuberances make the solid–liquid contact area larger than the apparent geometric contact area, which enhances the hydrophilicity geometrically. It is assumed that the liquid always fills the groove structure of the surface. The contact angle θ^* of a rough surface has the following relationship with the intrinsic contact angle θ_e of a smooth surface:

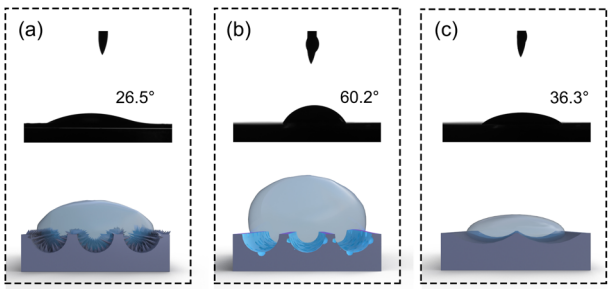

Fig. 4 Water droplets images and surface state schematic of anisotropic RCEs with rounding treatment durations of (a) 5 min, (b) 20 min and (c) 40 min.

$$\cos\theta^* = r(\gamma_{SG} - \gamma_{SL})/\gamma_{LG} = r\cos\theta_e \quad (2)$$

where r is the roughness factor representing the surface of the material, γ_{SG}, γ_{SL} and γ_{LG} are the specific surface energies of the solid–gas, solid–liquid and liquid–gas interfaces, respectively.

As the rounding reaction progresses, the density of the cutting marks decreases, and the nanopores that previously existed inside the cutting marks expand into a round hole structure. Air pockets appear inside cutting marks, which cannot be fully oxidized, thus exhibiting an intrinsic hydrophobic state. The state of surface contact turns into the Cassie model.[62,63] In the Cassie model, the contact of a droplet on a rough surface is compounded. The droplets on the hydrophobic surface cannot fill the grooves on the rough surface where there is trapped air. The apparent solid–liquid contact is composed of solid–liquid contact and gas–liquid contact. The change in surface Gibbs free energy, dG, can be described by the following formula:

$$dG = f_s(\gamma_{SL} - \gamma_{SG})dx + (1 - f_s)\gamma_{LG}dx + \gamma_{LG}\cos\theta^* dx \quad (3)$$

where f_s is the area fraction of the protruding solids in the composite contact surface.

At equilibrium, the apparent contact angle θ^* of a rough surface is the average value of the intrinsic contact angle θ_e of a smooth and flat surface and 180°, which has the following relationship:

$$\cos\theta_e^* = f_s(1 + r\cos\theta_e) - 1 \quad (4)$$

The air pockets can help to reduce the sliding angle. Due to the mechanical hindrance of the cutting mark to the sliding of the water droplet, only the sliding angle along the cutting mark direction is small. If the rounding treatment is further extended, the composite structure will be destroyed, and the contact angle and sliding angle will gradually tend toward the state presented by a smooth silicon surface. For a nearly smooth surface, IPA + KL-EPH cannot form an effective shield for any position in the hydrophilic treatment, so the entire surface is oxidized and becomes more hydrophilic.

Hydrophilic treatment also has a significant impact on the hydrophilicity of the sample. The contact angles and sliding angles of the sample with a rounding time of 20 min after different durations of hydrophilic treatment are shown in Fig. 5(a). The surface of the silicon wafer without hydrophilic treatment is in a hydrophobic state. As the hydrophilic reaction progresses, the water contact angle decreases, while the sliding angle gradually increases (as shown in Fig. 5(b)). When the hydrophilic treatment time exceeds 5 min, the sliding angle rises rapidly. Compared with the improved hydrophilicity, the resulting increase in the difficulty of water film desorption is not worth the loss for air–water extraction.

2.4 AWH performance

We selected a sample with a hydrophilic time of 5 min as the final RCE for the air–water extraction experiment. The EDS mapping results and XPS results of Si and O on the sample surface are shown in Fig. 5(c) and (d), respectively. After hydrophilic treatment, the bottom of the micro-groove was protected by IPA + KL-EPH from being oxidized, thus maintaining the intrinsic hydrophobic state. The raised parts on the sides of the micro-groove were oxidized, showing a hydrophilic state. The local difference in hydrophilicity and the oriented structure together create the unique water contact state of the RCE. Given that the RCE would be oxidized during the working process, a durability test was carried out. After 240 days of exposure to the open air, the oxygen content on the RCE surface changed by less than 5% (the relevant XPS results and sliding angle results are shown in Fig. S4). Accordingly, the sliding angle only increased by 3°.

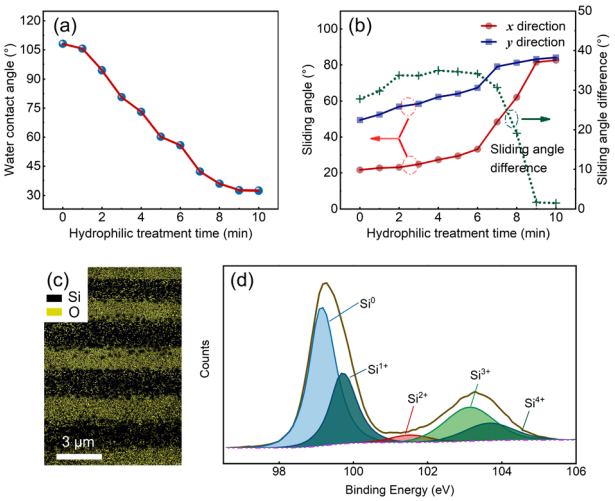

Fig. 5 Changes in the water contact angle (a) and water sliding angle (b) with hydrophilic treatment time; the dotted line in (b) is the difference in the water sliding angle in x and y directions. EDS mapping results of Si and O elements of RCE with hydrophilic treatment for 20 min are shown in (c); the corresponding XPS spectrum results are given in (d).

The AWH performance of the RCE was investigated. The photo of the experimental device is shown in Fig. 6(a). The RCE with a rounding time of 20 min was selected for the AWH experiment and placed in a thermal insulation box covered by Al foil to protect it from ambient heat radiation. The channels on the sidewalls of the box allowed air to enter and condensate water to flow out. The device was set on a holder that can freely adjust the inclination angle. For comparison, a sample with similar emissivity and water contact angle but no asymmetric sliding was employed in the control group (SEM images and the image of the water contact angle of the controlled RCE are shown in Fig. S5; the water sliding angle of the controlled RCE is 62°). The emissivity curve of RCE is shown in Fig. 6(b); the average emissivity of the RCE was about 0.86, while the average solar reflectivity was 0.12 within the solar wavelength spectra (0.3–2.5 μm). When the emitter inclination angle was 0, the experiment measured a temperature difference of 11.4 °C (Fig. 6(c)).

If the atmospheric emissivity is neglected, the absorption of environmental heat radiation by the RCE is 0 when $\alpha = 0$. If $\alpha >$

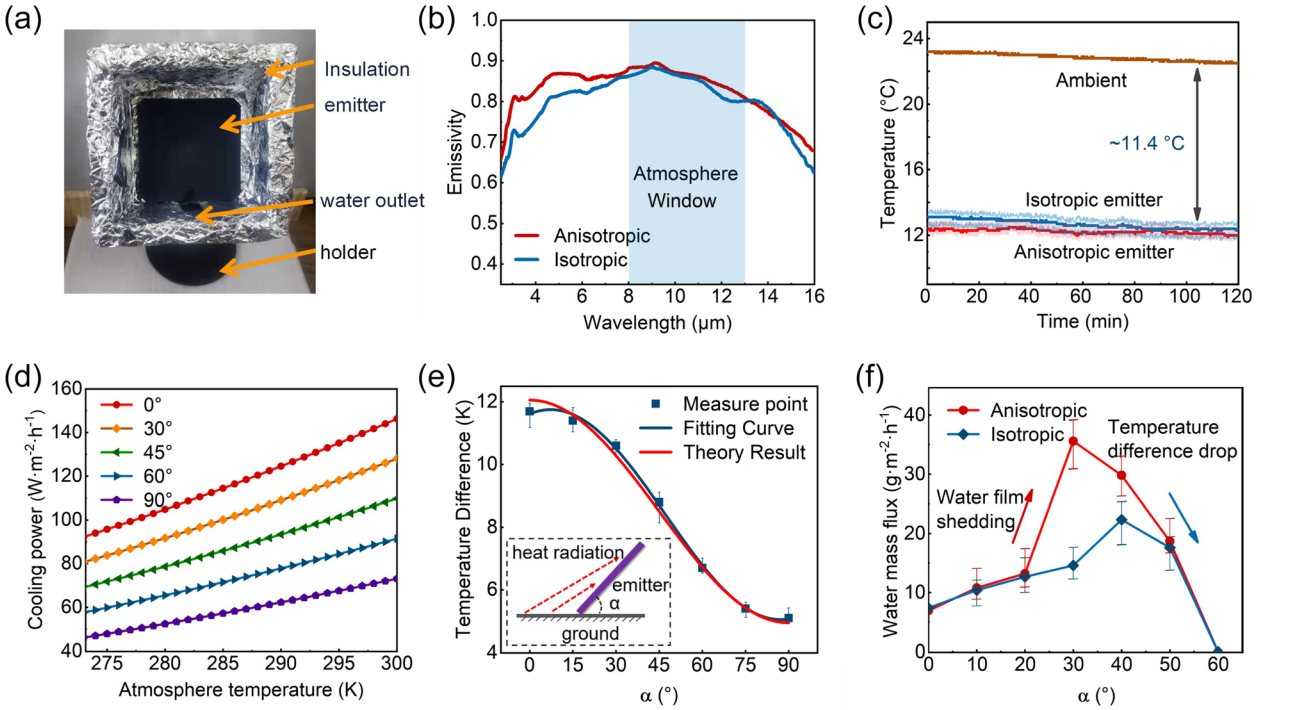

Fig. 6 (a) Photograph of the AWH experimental device; (b) emissivity curves of the anisotropic RCE for the experimental group and the isotropic RCE for the control group; (c) temperature curves of the anisotropic RCE and the isotropic RCE. The test was carried out under the conditions of $\alpha = 0$ and air humidity of 75%, in 20:00–22:00. (d) Radiative cooling power of ideal RCE at different α as a function of RCE temperature; (e) measurement results and theoretical results of radiative cooling temperature differences at different α; the inset shows the process of ambient thermal radiation absorbed by a tilted RCE. (f) Water mass fluxes of AWH based on the anisotropic RCE and the isotropic RCE at different α; the test was carried out under an air humidity of 75%, in 23:00–24:00. Error bars denote standard deviation ($n = 10$).

0, the RCE will absorb heat radiation from the ground. The absorption power is approximately equivalent to the radiative power of the RCE in the α range. The net cooling powers of the ideal RCE at various inclination angles were calculated, and the results are shown in Fig. 6(d). The calculation method is reported in our previous work.[64] The cooling power decays rapidly as the inclination angle increases, and the attenuation curve conforms to the law of cosine function (as shown in Fig. S6 in the SI). We measured the cooling temperature difference at various inclination angles. When $\alpha = 90°$, the cooling temperature difference is only 4.6 °C (Fig. 6(e)), which is less than half of that when $\alpha = 0$. It is worth noting that the actual RCE undergoes non-negligible non-radiative heat exchange with the surrounding environment; such an observed reduction aligns closely with theoretically predicted trends (the red line in Fig. 6(e)).

The water mass flux of AWH at different α is shown in Fig. 6(f). When α starts to increase from 0, the water mass flux gradually increases. Larger inclination angles will be of benefit to the partial shedding of the condensed water film, leading to an increase in water mass flux, but this increase is quite limited. When the inclination angle is smaller than the water sliding angle on the surface of the RCE, the water film cannot be completely separated from the RCE, which still hinders heat transfer. When α is greater than the sliding angle, water mass flux reaches the maximum. The sample from the experimental group reached the maximum water mass flux of 38.2 g m^{-2} h^{-1} when $\alpha = 30°$. The hydrophilic state of the RCE surface has a significant impact on its AWH performance. The water mass fluxes of anisotropic RCEs with different hydrophilic treatment durations are shown in Fig. S7. The specially optimized sample with the hydrophilic treatment time of 5 min achieved the best AWH performance. The control group needs a larger inclination angle to detach the water film, but increasing the inclination angle causes a decrease in the temperature difference of radiative cooling, which considerably weakens water vapor condensation. Therefore, the maximum water mass flux of the control group was only 22.3 g m^{-2} h^{-1}. The anisotropic RCE shows a clear advantage in AWH performance.

Although the RCE in this work has a high absorption of sunlight, the insulation box blocks part of the sunlight. Besides, the RCE has an inclination angle, so it can avoid direct sunlight in some situations. Fig. 7 shows the temperature curve, the temperature difference and the water mass flux of the RCE with an inclination of 30°, which were measured on June 07, 2021 (the solar power data is given in Fig. S8). Our RCE can maintain efficient radiative cooling from 18:00 to 8:00 the next morning. Following 8:00, the ambient heat radiation gradually increased, the cooling temperature difference decreased, and the water mass flux declined immediately until about 10:30 when the condensation of water vapor completely stopped. At 17:20, with the shifting of the sunlight and the weakening of ambient heat

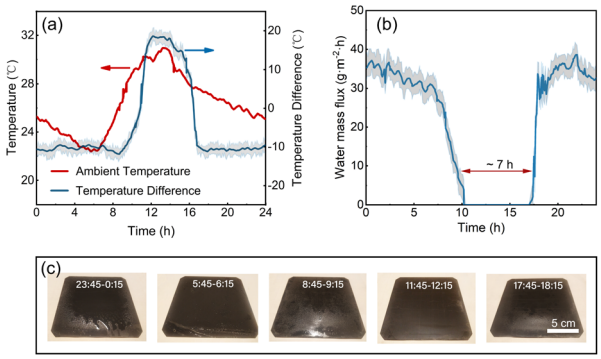

Fig. 7 (a) All-day ambient temperature curve and the radiative cooling temperature difference curve (June 07, 2021, Nanjing, China). (b) All-day water mass fluxes of AWH based on the anisotropic RCE (the test was carried out under outdoor conditions, with avg, max, and min air humidity of 73%, 68%, 78%, respectively). (c) Photographs of RCE after a working time of 30 min at different time periods. Error bars denote standard deviation ($n = 10$).

radiation, the temperature of the RCE again fell below the condensation point, so the air harvesting began. AWH disappears for 7 hours a day. Compared with the advantages of our anisotropic RCE in cost and accessibility, this efficiency loss is acceptable.

In addition to sunlight, air humidity and air temperature also affect the water mass flux of AWH; for related discussions, please see Fig. S9 and S10 in the SI. Pictures of RCE working for 30 min in different periods are shown in Fig. 7(c). Lots of water droplets were observed on the surface of the RCE, and they began to slide along the groove direction at 0:00 and 6:00. However, only a few water droplets adhered to the surface of the RCE at 9:00 and 18:00, which could not be collected by the spontaneous sliding of water droplets. At noon, the RCE temperature was higher than the ambient temperature, and no water droplets were formed on the surface of the RCE. The intrinsic properties of silicon-based microstructures limit the sample's reflectivity to sunlight (Fig. S10).

We have prioritized cost-effectiveness and scalability over absolute peak flux. Our emitter was fabricated using cheap industrial silicon wafers. The processes used in this work, including diamond wire-cut silicon substrates and metal-assisted chemical etching, are established mass-production processes in the photovoltaic industry, with a single-batch preparation yield of over 99%, which fully meets the requirements of large-scale replication and promotion. This enables large-scale deployment in resource-limited regions. We intentionally balanced spectral selectivity and surface properties to maintain low manufacturing complexity. Although our solar reflectivity is lower than that of some other RCEs, our system achieved comparable water-harvesting efficiency through optimized anisotropic droplet transport, as validated by the 71% performance gain over flat controls. Unlike lab-scale sorption systems that require complex regeneration processes, our passive radiative cooling design operates continuously without external energy input, making it suitable for off-grid applications.

3 Conclusions

In conclusion, the hydrophilicity of the RCE surface has a significant impact on water-harvesting performance. The hydrophilic surface is conducive to the nucleation of water droplets, but the water film adsorbed on the surface of the RCE will hinder the continuous progress of water harvesting. The MACE method and rounding process were employed to prepare composite micro-grooves + nano-pockets on a silicon wafer cut by diamond wire. The bottom of the micro-groove remains hydrophobic, and the top part is oxidized to stay hydrophilic throughout the local hydrophilic treatment. The microstructure introduces lots of air bubbles at the interface between the water droplet and the RCE, which greatly reduces the water sliding angle along the groove direction. As a result, an anisotropic water sliding RCE is obtained, while the hydrophilicity and low sliding angle are achieved at the same time. It has an emissivity of 0.86 and achieves a radiative cooling temperature difference of 11.4 °C at night. When the inclination angle is 30°, the maximum water mass flux is 38.2 g m^{-2} h^{-1}, which is a 71% increase compared to the control group, and it can work effectively for most of the day.

4 Methods

4.1 Radiative cooling emitter

Silicon wafers cut by diamond wire purchased from Trina Solar were employed as substrates after being cleaned using the standard cleaning processes. The silicon substrate was immersed in the $AgNO_3$ (0.02 mol L^{-1})/HF (4 mol L^{-1}) solution for 10 s to deposit Ag nanoparticles, then the silicon substrate was transferred to the HF (5.4 mol L^{-1})/H_2O_2 (3.5 mol L^{-1}) solution for 1 min. After removing the Ag nanoparticles, the substrate was placed in KOH (0.04 mol L^{-1})/NaF (0.16 mol L^{-1})/isopropyl alcohol (IPA, 5 vol%) for rounding treatment for 5–40 min under 35 °C. Next, the surface of the sample was coated with a mixed solution of IPA + ethylene glycol monophenyl ether (KL-EPH). Finally, a mixed solution of NH_3 H_2O (15 vol%)/H_2O_2 (15 vol%)/H_2O was used for hydrophilic treatment for 0–10 min.

4.2 RCE performance measurement

The emissivity tests were completed using an ultraviolet-visible-near infrared spectrometer (UV-vis-NIR spectrophotometer, Shimadzu, UV-3600, with an integrating sphere and a $BaSO_4$ plate as a reference, 0.3–2.5 μm) and a Fourier Infrared Spectrometer (FTIR, PerkinElmer, Frontier, with an integrating sphere coated by gold and a polished gold plate as a reference, 2.5–16 μm). The temperature of each layer was recorded using a dual-channel automatic temperature measuring device (GSP-6, Elitech). Considering the variability of the ambient temperature, the ambient temperature in this work refers to the air temperature at the same height as the RCE from the ground. The model of the scanning electron microscope was LYRA3 TESCAN. The surface roughness information described in this work was obtained by a Dimension FastScan (Bruker). The model of the contact angle measuring instrument was XBR-

2100. The testing equipment for the sliding angle was home-designed and manufactured, and water drops of 0.02 mL were used in all sliding angle measurements.

4.3 Outdoor experimental setup

For all outdoor experiments, 10 groups of samples were set up and tested simultaneously in the same environment to ensure data reliability. To guarantee that both the anisotropic emitter and control samples experienced identical convective environments, synchronous co-located testing was carried out: all samples with the same heat preservation setting were mounted on the same test platform, placed side-by-side with 30 cm spacing, ensuring they were exposed to the same ambient airflow and temperature fluctuations simultaneously. To mitigate the interference of intense air convection on the experimental outcomes, our setup was outfitted with thermal insulation films and foam enclosures, which ensured that the air within the device remained in a quasi-static state, isolated from ambient convective effects. AWH measurement was carried out outdoor on a wind-free sunny day. (0–24 h, 25 ± 2 °C, RH 73% $\pm$ 5%, wind speeds 0.4 ± 0.1 m s^{-1}, dew points 17 ± 1 °C).

4.4 Water mass flux

A precision electronic scale (Puchun, JY3002) with a resolution of 0.01 g was employed to measure the water harvesting mass. The water harvesting mass was recorded as m_1 at time t_1 and m_2 at t_2; then, we got the water mass flux as $F_w = \frac{m_2 - m_1}{t_2 - t_1}$. The time interval of data recording is 5 min.

Author contributions

Conceptualization: Kai Gao and Jiajia Wu; methodology: Kai Gao; investigation: Kai Gao, Jiajia Wu, Jinze Li; resources: Kai Gao, Jinze Li, luanhong Sun; data curation: Kai Gao, Jiajia Wu; writing-original draft preparation: Kai Gao; writing-review and editing: Jiajia Wu, Jinze Li; supervision: Luanhong Sun; project administration: Jiajia Wu; and funding acquisition: Jinze Li.

Conflicts of interest

There are no conflicts to declare.

Data availability

The data that support the findings of this paper are available from the corresponding author, Jiajia Wu, upon reasonable request.

The data supporting this article have been included as part of the supplementary information (SI). Supplementary information is available. See DOI: https://doi.org/10.1039/d5ra09103a.

Acknowledgements

This work has been financially supported by the National Natural Science Foundation of China (61774084).

Notes and references

1 M. Kummu, P. J. Ward, H. D. Moel and O. Varis, *Environ. Res. Lett.*, 2010, **5**, 034006.
2 M. Elimelech and W. A. Phillip, *Science*, 2011, **333**, 712–717.
3 J. Guo, Z. D. Tucker, Y. Wang, B. L. Ashfeld and T. Luo, *Nat. Commun.*, 2021, **12**(1), 437.
4 R. Li and P. Wang, Sorbents, *Nat. Water*, 2023, **1**, 573–586.
5 Y. Zhong, L. Zhang, X. Li, *et al.*, *Nat. Rev. Mater.*, 2024, **9**(10), 681–698.
6 Z. Ahrestani, S. Sadeghzadeh and H. B. M. Emrooz, *RSC Adv.*, 2023, **13**, 10273–10307.
7 H. L. Nguyen, *Adv. Mater.*, 2023, **35**, 2300018.
8 Y. Wu, H. Li, L. Wen, D. Men, L. Hang, D. Liu, G. Liu, W. Cai, X. Lyu and Y. Li, *Surg. Innov.*, 2018, **6**, 141–149.
9 A. Mulchandani, S. Malinda, J. Edberg and P. Westerhoff, *Environ. Sci. Nano*, 2020, **7**, 2584–2594.
10 B. Zhao, L. Wang and T. Chung, *Sep. Purif. Technol.*, 2019, **220**, 136–144.
11 J. E. Arias-Torres and J. J. Flores-Prieto, *Atmosphere*, 2015, **7**, 2–13.
12 A. Lee, M. W. Moon, H. Lim, W. Kim and A. H. Kim, *Langmuir*, 2012, **28**, 10183–10191.
13 Y. Tu, R. Wang, Y. Zhang and J. Wang, *Joule*, 2018, **2**, 1452–1475.
14 D. P. Cox and W. H. Tucker, *Astrophys. J.*, 1969, **157**, 1157.
15 M. Lee, G. Kim, Y. Jung, *et al.*, *Light: Sci. Appl.*, 2023, **12**, 134.
16 X. Zhao, T. Li, H. Xie, *et al.*, *Science*, 2023, **382**, 684–691.
17 C. Lin, K. Li, M. Li, *et al.*, *Adv. Mater.*, 2025, **37**, 2409738.
18 F. Xie, W. Jin, J. R. Nolen, *et al.*, *Science*, 2024, **386**, 788–794.
19 T. Nilsson, W. E. Vargas, G. A. Niklasson and C. G. Granqvist, *Renew. Energy*, 1994, **5**, 310–317.
20 O. Clus, P. Ortega, M. Muselli and I. Milimouk, *J. Hydrol.*, 2008, **361**, 159–171.
21 A. Jacobs, B. Heusinkveld and S. Berkowicz, *Atmos. Res.*, 2008, **87**, 377–385.
22 I. Haechler, H. Park, G. Schnoering, T. Gulich, M. Rohner, A. Tripathy, A. Milionis, T. M. Schutzius and D. Poulikakos, *Sci. Adv.*, 2021, **7**, eabf3978.
23 J. Wu, X. Xia, X. Du, T. Ma, T. Jia and S. Liu, *Appl. Therm. Eng.*, 2024, **245**, 122791.
24 S. Ahmad, A. R. Siddiqui, K. Yang, M. Zhou, H. M. Ali, R. Hardian, G. Szekely, D. Daniel, S. Yang and Q. Gan, *Adv. Mater.*, 2024, **36**, 202404037.
25 Y. Zheng, H. Bai, Z. Huang, X. Tian, F. Nie, Y. Zhao, J. Zhai and L. Jiang, *Nature*, 2010, **463**, 640–643.
26 J. Xu, X. Huo, T. Yan, P. Wang, Z. Bai, J. Chao, R. Yang, R. Wang and T. Li, *Energy Environ. Sci.*, 2024, **17**, 4988–5001.
27 Y. Huang, Q. Li and Z. Chen, *J. Colloid Interface Sci.*, 2024, **655**, 527–534.
28 W. Zhu, Y. Zhang, C. Zhang, X. Shan, A. K. Rao, S. L. Pitts, *et al.*, *Commun. Eng.*, 2023, **2**, 35.

29 Y. Zhang, W. Zhu, C. Zhang, J. Peoples, X. Li, A. L. Felicelli, X. Shan, D. M. Warsinger, T. Borca-Tasciuc, X. Ruan and T. Li, *Nano Lett.*, 2022, **22**, 2618–2626.
30 A. Shastri, J. Nirmalkar, S. Kim, S. Oh, K. Lee and M. Song, *ACS Earth Space Chem.*, 2025, **9**, 1768–1779.
31 J. Nirmalkar, J. Y. Lee, K. Lee, J. Ahn and M. Song, *ACS Earth Space Chem.*, 2025, **9**, 1256–1266.
32 X. Zhao, C. M. Pavuluri, Z. Dong, Z. Xu, J. Nirmalkar, J. Jung, F. Pingqing and C. Q. Liu, *J. Geophys. Res. Atmos.*, 2023, **128**, e2023JD038864.
33 J. Nirmalkar, K. Lee, J. Ahn, J. Lee and M. Song, *Atmosphere*, 2023, **14**, 753.
34 J. Nirmalkar, J. Jung, S. Han, Z. Dong, Z. Xu, P. Fu and C. M. Pavulari, *Atmos. Environ.*, 2023, **293**, 119457.
35 J. Nirmalkar, D. Haswani, A. Singh, S. Kumar and R. S. Raman, *J. Environ. Manag.*, 2021, **293**, 112904.
36 J. Nirmalkar, R. Sunder Raman, D. K. Deshmukh and M. D. M. Haque, *Atmos. Environ.*, 2023, **294**, 119516.
37 S. V. Boriskina, A. Raza, T. Zhang, P. Wang, L. Zhou and J. Zhu, *MRS Bull.*, 2019, **44**, 59–66.
38 C. Liu, Y. Wu, B. Wang, C. Y. Zhao and H. Bao, *Sol. Energy*, 2019, **183**, 218–225.
39 D. Beysens, M. Muselli, I. Milimouk, C. Ohayon, S. M. Berkowicz, E. Soyeux, M. Mileta and P. Ortega, *Energy*, 2006, **31**, 2303–2315.
40 T. Nilsson, W. E. Vargas, G. A. Niklasson and C. G. Granqvist, *Renew. Energy*, 1994, **5**, 310–317.
41 A. R. Parker and C. R. Lawrence, *Nature*, 2001, **414**, 33–34.
42 X. Dai, N. Sun, O. N. Steven, B. B. Stogin, J. Wang, S. Yang and T. S. Wong, *Sci. Adv.*, 2018, **4**, eaaq0919.
43 M. J. Kreder, J. Alvarenga, P. Kim and J. Aizenberg, *Nat. Rev. Mater.*, 2016, **1**, 1–15.
44 J. Long, P. Fan, D. Jiang, J. Han, Y. Lin, M. Cai, H. Zhang and M. Zhong, *Adv. Mater. Interfac.*, 2016, **3**, 1600641.
45 L. Cao, A. K. Jones, V. K. Sikka, J. Wu and D. Gao, *Langmuir*, 2009, **25**, 12444–12448.
46 L. Zhai, M. C. Berg, F. C. Cebeci, Y. Kim, J. M. Milwid, M. F. Rubner and R. E. Cohen, *Nano Lett.*, 2006, **6**, 1213–1217.
47 S. Ozden, L. Ge, T. N. Narayanan, A. Hart, H. Yang, S. Sridhar, R. Vajtai and P. M. Ajayan, *ACS Appl. Mater. Interfaces*, 2014, **6**, 10608–10613.
48 X. Zeng, L. Qian, X. Yuan, C. Zhou, Z. Li, J. Cheng, S. Xu, S. Wang, P. Pi and X. Wen, *ACS Nano*, 2017, **11**, 760–769.
49 N. Suzuki, T. Makino, Y. Yamada, T. Yoshida and S. Onari, *Appl. Phys. Lett.*, 2000, **76**, 1389–1391.
50 K. X. Wang, Z. Yu, V. Liu, Y. Cui and S. Fan, *Nano Lett.*, 2012, **12**, 1616–1619.
51 V. Garg, R. G. Mote and J. Fu, *Opt. Mater.*, 2019, **94**, 75–85.
52 H. Park, M. Ju, M. Q. Khokhar, E. C. Cho and J. Yi, *Trans. Electr. Electron. Mater.*, 2020, **21**, 349–354.
53 M. Seo, S. Yoon, H. Cho, S. Lee, K. Kim, B. D. Kong and M. Meyyappan, *IEEE J. Photovolt.*, 2020, **10**, 475–479.
54 G. Sahu and G. S. Okram, *Silicon*, 2021, **13**, 3865–3870.
55 D. Zhang, S. Jiang, K. Tao, R. Jia and Z. Jin, *Sol. Energy Mater. Sol. Cells*, 2021, **230**, 111200.
56 H. Li, Q. Wang, C. Jian, J. Krc and W. J. Soppe, *Opt. Commun.*, 2012, **285**, 808–815.
57 F. A. Martinsen, B. K. Smeltzer, J. Ballato, T. Hawkins, M. Jones and U. J. Gibson, *Opt. Express*, 2015, **23**, A1463–A1471.
58 Y. Shen, C. W. Hsu, Y. X. Yeng, J. D. Joannopoulos and M. Solja, *Appl. Phys. Rev.*, 2016, **3**, 1637–1679.
59 Z. Huang, N. Geyer, P. Werner, J. D. Boor and U. Gösele, *Adv. Mater.*, 2011, **23**, 285–308.
60 H. Han, Z. Huang and W. Lee, *Nano Today*, 2014, **9**, 271–304.
61 C. Rohrs, A. Azimi and P. He, *Langmuir*, 2019, **35**, 15421–15430.
62 C. Lee, Y. Nam, H. Lastakowski, J. I. Hur, S. Shin, A. Biance, C. Pirat and C. Ybert, *Soft Matter*, 2015, **11**, 4592–4599.
63 B. E. Young and B. N. Wenzel, *Colloids Surf., A*, 2009, **345**, 163–165.
64 K. Gao, Y. Liu and H. Shen, *J. Photon. Energy*, 2021, **11**, 022102.